

DESIGN AND SIMULATION OF A BLOWING AND SUCTION WIND TUNNEL FOR CORNERING EFFECT

Yeung Chak Hoi Wisely

Department of Aerospace Engineering, University of Bristol, Queen's Building, University Walk,
 Bristol, BS8 1TR, UK

Abstract

Aerodynamic analysis of vehicles in the cornering condition is a key design parameter especially in the motorsport industry. Yet, it has proven difficult to be accurately recreated experimentally due to the complexity of modelling curved flow. This paper is the first to propose the idea of a blowing and suction wind tunnel. Based on the rectangular numerical domain, blowing and suction slots are placed on the sidewalls of the test section. Different cornering radii can be replicated through altering mass flow rates. Performances on an aerofoil and an F1 race car were simulated and validated against the idealised rotating domain, with investigations on different turning angles and the number of slots. Through analysing mainly the force coefficients, pressures at and away from the surface, and the simulated radii, it demonstrated more accurate modelling with a greater number of slots and a more relaxed cornering curvature. Significant improvement was shown after taking into account the turbulent flow mixing effect in mass flow rate values.

Keywords: Cornering, Wind Tunnel, Computational Fluid Dynamics, Blowing and suction

1 INTRODUCTION

Cornering condition is a crucial design parameter of vehicles, particularly in the motorsport industry. Racing cars must maintain their stability when executing different types and curvatures of corners, whilst competing with dirty flow generated by contestants. To achieve a stable cornering performance, racing car components are often designed to maximise downforce even though their top speed is compromised. Therefore, it is important to replicate on-track cornering phenomena during the designing phase to optimize their performances.

Figure 1 demonstrates the flow characteristics of a vehicle in a steady-state cornering condition. Inner and outer flow field velocities, U_1 and U_2 , vary differently along the span, with a larger U_2 resulting from a greater distance away from the centre of rotation. Static pressures, P_1 and P_2 , remain constant across the domain. Front and rear parts experience opposite yaw angles ψ as the vehicle rotates about its centre of gravity. In the reference frame of the vehicle body, the flow field is observed to pass over the body following the same cornering path [17]. Thus, it is interpreted as a curved fluid flow around a static vehicle. In practice, cornering conditions vary with different vehicle designs and drivers. For instance, drivers with different preferences in corner entries result in different slip angles.

To simulate vehicles' aerodynamic performances, Computational Fluid Dynamics (CFD) software and wind tunnels are usually used during the development stage. Wind tunnel testing, in particular, plays an important role in terms of validating early-stage design parameters and bringing an accurate correlation between CFD results and on-track performance, which is a crucial aspect of cornering. Several experimental wind tunnel testing methods, such as the NASA Langley Stability Tunnel [5], the bent model [24, 12, 13] and the Whirling Arm [19] were previously dedicated to cornering

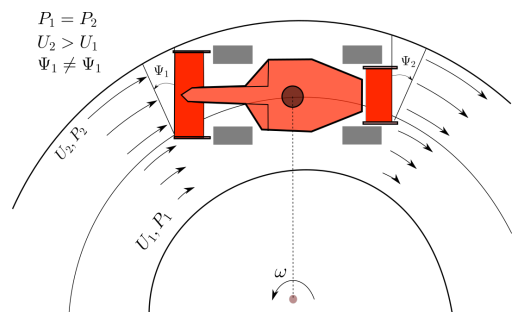


Figure 1: Steady-state cornering flow conditions

effect investigations. However, they were concluded to be physically limited in different ways. Moreover, they were all designed and built for one distinct turning angle only. It is both time- and cost-ineffective to adapt all cornering conditions based on these pre-existing methods.

At present, due to the lack of wind tunnel facilities, Formula 1 (F1) teams rely heavily on CFD for cornering flow analysis. Several studies [21, 17, 16, 22, 25] proposed various methods in modelling boundary conditions and the structure of fluid domain in CFD cornering simulation. Nevertheless, CFD is only a simplification of the actual fluid behaviour. Cornering involves a highly complex turbulent flow. It is computationally expensive to solve the Navier-Stokes equation to properly simulate the entire turbulent flow behaviour. Therefore, wind tunnel technologies are crucial for modelling the cornering effect in physically replicating turbulent performances and validating idealised aerodynamic parameters of racing cars.

The aim of this study is to design and simulate a wind tunnel incorporating blowing inlets and suction outlets on the sidewalls, so that it can replicate various cornering conditions by simply altering the mass flow rates of boundary conditions. The long-term vision is to provide an experimental solution for the motorsport industry in accurately modelling racing cars' cornering performances, especially accounting for the turbulent flow. Regarding this, a symmetrical aerofoil and an F1 car model are placed under blowing and suction, with results validated against the idealised rotating domain. The simple aerofoil simulation is used to establish a basic understanding of the tunnel configuration and obtain data in less time. The more complex F1 car simulation is done to fulfil the intended purpose of this wind tunnel. Simulation performances under different number of channels and turning curvatures are explored, with an analysis of different aerodynamic parameters.

1.1 PREVIOUS WORK AND RESULTS

1.1.1 Experimental Methods for Cornering

Langley Stability Tunnel The Langley Stability Tunnel is a curved wind tunnel built by the NASA Langley Research Centre in 1939, designed to be capable of testing an aircraft in rolling, pitching and yawing [5]. Test sections are interchangeable, allowing curved sidewalls to be installed. However, when the fluid flow is forced into the curved section, the concave outer wall causes the flow to decelerate, resulting in a pressure increase. An opposite effect in flow acceleration and pressure drop is caused by the convex inner wall. Hence, the angular momentum of the air tends towards the outer wall, resulting in an uneven variation in static pressure distribution across the test section, which does not replicate the actual cornering situation. The sidewall effect is further amplified under tighter curved curvatures, increasing the error in capturing aerodynamic properties.

The Bent Model The bent model is a different approach proposed in several studies [24, 12, 13], in which instead of creating a curved flow, the test object is curved relative to a straight freestream flow. It is cost-beneficial as modelling can be done using any straight channel wind tunnels. Nevertheless, since the outer span of the test object is longer than the inner span, bent modelling results in a lower Reynolds number on the outboard, which is the opposite case of actual cornering. Moreover, while vehicles are in motion, it is unrealistic to model rotating curved wheels to mimic the curved flow thoroughly. Therefore, it is not practically used in cornering simulation.

Whirling Arm In 1908, a whirling arm was built in the National Physics Laboratory (NPL) in the UK [19]. It was introduced by Benjamin Robins in 1746, in which the test object is fixed at one end of a metal arm, and the other end fixed at the pivot to spin in a circular path. Assuming air within the test section is stationary, the circular motion of the test object passing through still air is a perfect replication of the cornering condition. However, after completing each rotation, the test object is subsequently travelling in the wake created from the previous lap. This leads to the generation of a vast amount of unwanted turbulence and swirls.

Yawed car in straight wind tunnel The current method of estimating cornering effects by F1 teams is to place a yawed car model in a straight wind tunnel at several angles. Each yaw angle is then combined into frames of motion to mimic the yaw rate during a corner. However, it is acknowledged that the yawed car method can only simulate the side-slip angle effect since straight wind tunnels only produce straight freestream, which cannot mimic curved flow in an actual corner. Subsequently, data obtained must be calibrated and reported as estimates.

1.1.2 Numerical Methods for Cornering

Boundary Configuration In general, the numerical domain is defined as a non-inertial reference frame, in which the angular motion is prescribed as an angular velocity about a fixed centre of rotation located outside of the domain. This represents a steady-state corner with constant radius [16].

In a previous study of unsteady aerodynamics of vehicles [21], it implemented the dynamic motion of the vehicle through the mesh instead. It can reduce the computational cost required for the Coriolis term and acceleration terms associated with the non-inertial reference frame. However, additional modelling in the inlet and outlet boundary conditions is required. Therefore, the non-inertial reference frame is adopted in this research instead.



Figure 2: Numerical methods for cornering

Curved Domain During a corner, the flow is observed to pass over the vehicle body following the same curved path. Thus, the cornering effect can be modelled by applying the concept of the curved domain as shown in Figure 2a. In practice, each mesh simulation only corresponds to one specific cornering condition under the curved domain. Generating a mesh for every desired angle is computationally expensive and time-consuming. Moreover, similar to the Langley Stability Tunnel, undesired sidewall effects arise due to pressure variations across inner and outer walls [17].

Rectangular Domain The rectangular domain was proposed by several studies in the past [22, 25], with the concept shown in Figure 2b. The mesh rotates about the origin of the rotational frame of reference under the rectangular domain. It consists of three inlets and outlets. Modifying the inlet and outlet conditions allows simulation of a curved flow with different combinations of curvatures and speeds using the same mesh. It reduces computational requirements and costs to obtain aerodynamic properties for various angles and entry velocities, as well as avoiding undesired curved wall effects. This in theory fully replicates the flow field of a cornering vehicle.

1.1.3 Perforated Walls in Wind Tunnels

The proposed idea of multiple blowing and suction channels was inspired by the transonic wind tunnel. Its distinct feature of the openings in the sidewalls of the test section allows fluid flow to be relieved from the choking effect.

In 1946, Ray Wright [4] analysed the potentialities of introducing openings in the test section walls, called the slotted

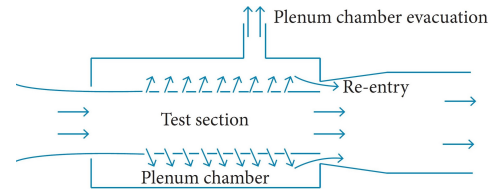


Figure 3: Transonic wind tunnel showing the system of forced extraction and re-entry flaps. [11]

or perforated walls, as illustrated in Figure 3. Unwanted aerodynamic distortions are alleviated or delayed by the presence of the sidewall openings. A portion of the main flow is extracted by auxiliary compressors into the plenum chamber, which is isolated from the test section. It is then reintroduced back into the main flow circuit at the test section outlet where the stream speed is low enough to avoid undesirable turbulent losses [11].

With the success of the plenum chamber implementation, this research suggests the plausibility to implement blowing and suction channels at the desired openings in the sidewalls of the wind tunnel. Auxiliary compressors can be used to adjust mass flow rates and introduce them into the test section via blowing and suction channels.

2 METHODOLOGY

2.1 Concept wind tunnel design

Figure 4 showcases the concept design for the implementation of blowing and suction components to a closed circuit wind tunnel. Blowing and suction make use of the idea of closed-loop circuits surrounding the test section, connecting both sidewalls via several ducts shown in Figure 4b. A variable speed fan is implemented inside each duct to facilitate blowing on one side and suction on the other side, as well as flow speed control. Surrounded side duct placements can make efficient use of the open space of pre-existing closed circuit wind tunnels. The gravity effect in the vertical sections of the side ducts were assumed to be negligible in this paper.

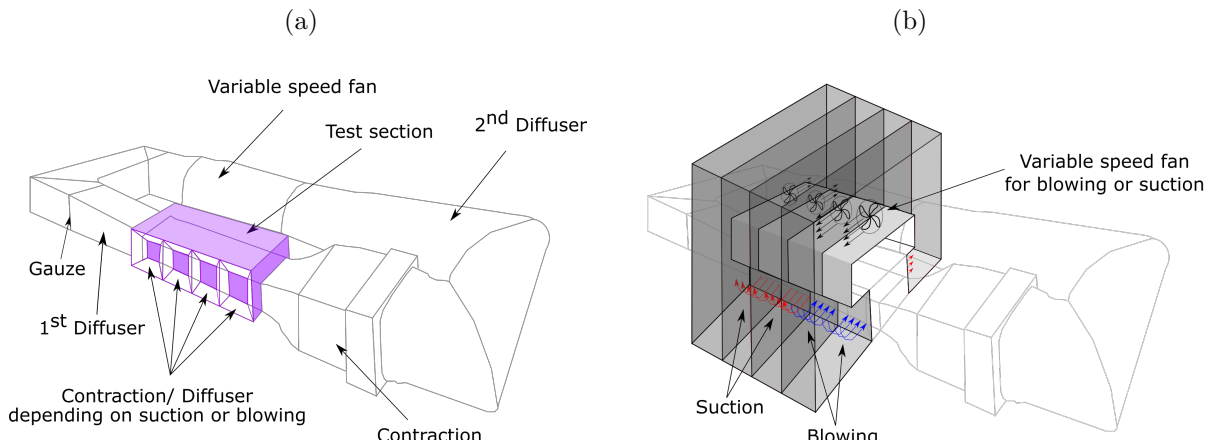


Figure 4: Blowing and suction wind tunnel concept design: (a) Conventional wind tunnel with contraction and diffusers at sidewalls, (b) Implementation of blowing and suction channels
(Diagrams are NOT drawn to scale)

At the connection junction of the sidewalls, additional contractions and diffusers are implemented, as shown in Figure 4a. Similar to those in the main wind tunnel, contractions are responsible for accelerating the inflow and enforcing laminar flow, whereas diffusers recover static pressure in order to increase the wind tunnel's efficiency and prevent backflow to the test section [14].

Dimensions of the blowing and suction ducts used in this paper were estimated based on the Toyota Motorsport GmbH (TMG) wind tunnel [20]. The length of the test section is approximately 10~12m. Allocating 8 ducts on one side, with each duct width around 1~1.5m is considered to be a reasonable estimation for the maximum number of slots. This allows the installation of propeller fans with a diameter of around 0.8~1.3m, expected to accelerate the flow speed up to half of the inlet flow speed. Further increasing the number of channels will result in an overly complex mechanism in construction.

2.2 NUMERICAL AND BOUNDARY CONDITION (WIND TUNNEL MODELLING)

Two techniques were used to recreate cornering motions during flow simulations. One is the fixed frame of reference with blowing and suction, in which the coordinate frame is fixed at the centre of gravity of the model. The radial acceleration of the vehicle is reproduced by the external blowing and suction. The other is the Arbitrary Lagrangean-Eulerian (ALE) method [15]. It transforms the Navier-Stokes equation to allow simulation in a moving domain. It is adopted in a non-inertial reference frame, which is the idealised domain for validating the blowing and suction method.

2.2.1 Fixed frame of reference with blowing and suction

In the blowing and suction simulation, the reference frame coordinate for calculating the fluid motion is fixed at the centre of gravity of the test object. The corresponding lateral velocity is given by the crosswind acting on the test object. Averaged corresponding blowing and suction velocities are then introduced on two sides of the domain. This computational representation is demonstrated in Figures 5a and 5b, where constant mass flow rates are introduced at the inlet, with blowing and suction channels allocated on the two sides. Simple gradient-free and slip boundary conditions were applied at outlets and the ceiling. Reynolds numbers of the flow were set to match with the idealised reference frame in Section 2.2.2.



Figure 5: Numerical domain for blowing and suction channels: (a) Isometric view, (b) Top view
(Arrows are NOT drawn to scale)

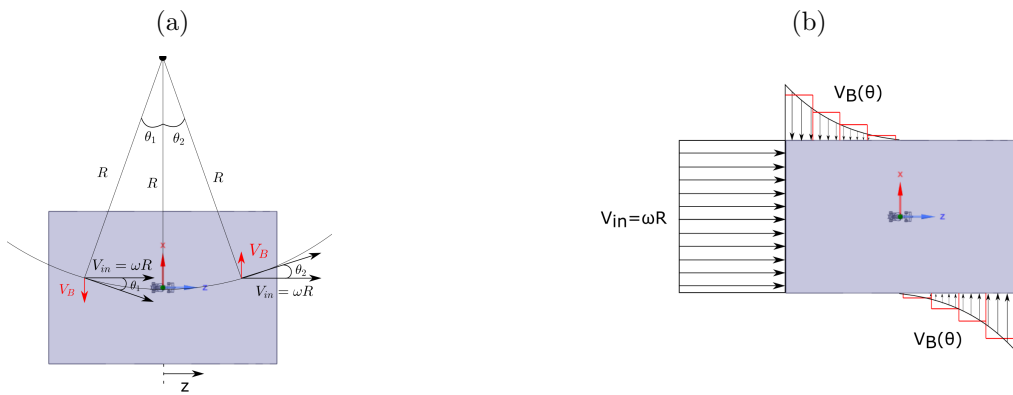


Figure 6: Graphical representations for the blowing and suction wind tunnel: (a) Velocity profile for the numerical domain, (b) Velocity components of a vehicle following a curved path

Velocity of the inlet V_{in} is configured using the tangential velocity component ωR of the vehicle about the desired referenced origin. Moreover, input parameters for blowing and suction boundary conditions are obtained by resolving vertical velocity components (Equation 1) when a vehicle is following a circular path denoted in Figure 6a.

$$V_B = \omega R \tan(\theta) = \omega R \left(\frac{\sin(\theta)}{\sqrt{1 - \sin^2(\theta)}} \right) \quad (1)$$

From geometry, the displacement z along the length of the domain is obtained by Equation 2.

$$z = R \sin(\theta) \quad (2)$$

After substituting the expression of z back into Equation 1, the velocity profile shown in Figure 6b is derived from applying the Taylor's Series expansion (Equation 3). It results in an odd function, proving the anti-symmetry of the velocity profile about the vertical axis. The velocity profile tends to be linear for small $\frac{z}{R}$ and behaves in a cubic manner for larger $\frac{z}{R}$.

$$V_B = \omega R \left(\frac{z/R}{\sqrt{1 - (z/R)^2}} \right) = \omega R \left(\left(\frac{z}{R} \right) + \frac{1}{2} \left(\frac{z}{R} \right)^3 + \frac{3}{8} \left(\frac{z}{R} \right)^5 + \dots \right) \quad (3)$$

The displacement z is divided into N blowing and suction slots. The velocity for each individual slot V_B^n is averaged across the start and end positions of each slot (Equation 4). By doing so, the theoretical smooth velocity profile is discretised into N step-wise constant velocity values, demonstrated by the red lines in Figure 6b.

$$V_B^n = \omega \left(\frac{\left(\frac{z_i^n + z_{i+1}^n}{2} \right)}{\sqrt{1 - \left(\frac{z_i^n + z_{i+1}^n}{2R} \right)^2}} \right) \quad (4)$$

The mass flow rate \dot{m}_B^n , which is the final input value of each blowing and suction slot, is then obtained by the product of air density ρ , cross-sectional area A and V_B^n of each slot shown in Equation 5. Suction outlets are placed opposite to the blowing inlets, with the same magnitude of mass flow rates for each opposite pair. The sum of mass flowing in is equal to the sum of mass flowing out at each time step iteration, characterising the global incompressible flow.

$$\dot{m}_B^n = \rho A_{slot} V_B^n = \rho A_{slot} \omega \left(\frac{\left(\frac{z_i^n + z_{i+1}^n}{2} \right)}{\sqrt{1 - \left(\frac{z_i^n + z_{i+1}^n}{2R} \right)^2}} \right) \quad (5)$$

In this research, an aerofoil and an F1 car model were placed under simulation with a rotation velocity ω of 5 rpm. Based on the length of the test section mentioned in Section 2.1, 4 and 8 blowing and suction slots were first integrated on each side to compare their simulation accuracies under a cornering chord-to-radius ratio (z/R) of 0.10. In order to reduce computational expenses, an 8-slot numerical mesh was used in both simulations, in which to mimic the 4-slot condition, neighbouring slots were paired up and given the same input conditions. After deducing the most suitable number of slots, the simulation performance of a tighter corner ($z/R = 0.15$) was tested. Combinations between chord-to-radius ratios and the rotational velocity were chosen statistically based on the average speed of F1 on The Marina Bay Street Circuit and The Hungaroring Track from 2009 to present [1]. Aerodynamic parameters including pressure coefficients, total drag and downforce coefficients, and vortex visualisation were used for accuracy analysis.

2.2.2 Idealised non-inertial (rotating) frame of reference (Reference for Validation)

The non-inertial rotating mesh refers to the rectangular domain mentioned in Section 1.2.2, which is considered ideal as it is theoretically identical to the actual cornering motion with constant static pressure across the mesh. Therefore, it was used to validate the above blowing and suction method

in all simulation conditions, in which a blowing and suction simulation is considered to be more accurate if the obtained aerodynamic properties are closer to that of this rotating simulation.

The radial acceleration is reproduced by the external force from the Navier-Stokes equations (Equations 9, 10, 11). Figures 7a and 7b show the computational representation of this reference frame. Sidewalls were modelled as pressure inlets and outlets with a static pressure of 0 Pa, theoretically not creating any interference between inflow, outflow and the model under investigation. Simple gradient-free and slip boundary conditions were imposed at outlets and the ceiling. Reynolds numbers of the flow were set to vary with respect to freestream velocities, theoretically matching with that in actual cornering, allowing boundary layers modelling on the ground and model surfaces.



Figure 7: Numerical domain of non-inertial frame of reference: (a) Isometric view, (b) Top view

2.3 GEOMETRY OF AEROFOIL AND VEHICLE MODEL

As mentioned in Section 1, an aerofoil model and an F1 car model were used as test objects in cornering simulations. Both of their computational domains had a dimension of $9L \times 6L \times 1.5L$, as displayed in Figure 8b and Figure 9c, with L being the length of the model. This provides a front/back clearance of $4L$ to both the leading and trailing surfaces of the model from the inlet and outlet wall correspondingly. The clearance allows the after-body aerodynamics to be fully captured. A side clearance of $2.9L$ would be wide enough to prevent the direct impact of the blowing effect between opposite walls.

2.3.1 2D - Aerofoil geometry model

The symmetrical aerofoil NACA 0012 was modelled with no tapering and 0° angle of attack to obtain 2D results across the wingspan. The CAD model for this aerofoil with a length (L) of 0.1m is shown in Figure 8a. It was placed under the domain with its cross-sectional chord oriented upwards towards the ceiling, as shown in Figure 8b. As the chord-wise effect is more significant than the span-wise effect, aerodynamic changes will be more apparent under blowing and suction, obtaining a more sensitive analysis.

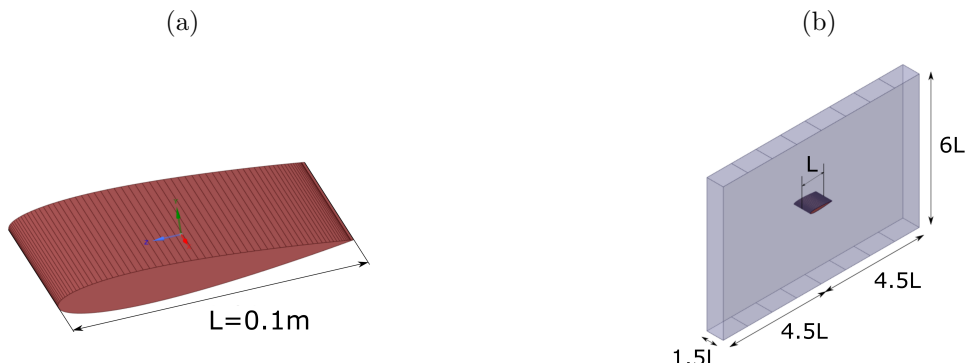


Figure 8: Geometries of the aerofoil: (a) 3D NACA 0012, (b) Domain enclosure for aerofoil

2.3.2 3D - F1 racing car geometry model

The vehicle model and its associated components are shown in Figure 9. It was constructed under the influence of the Fédération Internationale de l'Automobile (FIA) regulations, such that its characteristics would be common to most categories of Formula racing cars, including a model length (L) of 4.736m. All aerodynamic analysis was done with the projected frontal area of 1.27 m^2 , which is similar to the standard dimension in F1. The model was oriented to be tangent to the centre of rotation (Figure 1).

Aerodynamic properties of the front wing and the rear wing were the main focus of this research, with their geometries described in Figure 9d, e. The front wing consisted of a single inverted cambered aerofoil which is commonly used in the automotive industry. Inverted aerofoils are capable of producing downforce to stabilise ground vehicles in motion. The rear wing was made of a double-element aerofoil and a set of double beam wings, which the latter was not considered in the aerodynamic analysis since it is heavily affected by the upstream components.

Between the wheel and the ground of the domain, a contact patch with a curvature of 8mm was added, as shown in Figure 9f. The use of contact patches was investigated by Sammy Diasinos [10]. Besides reducing the skewness in model mesh, they can also model the deformation of tires due to the weight and the motion of the car.

To reduce the model complexity for the CFD solver and facilitate a clearer observation of components that could interfere with each other, simplification of the car model was done by a few modifications. The airbox inlet of the engine intake above the driver was blocked off. Each side pod was modelled as a straight pipe without modelling the engine cooling effect. Sharp angles were rounded to avoid skewness in the discretising stage. Furthermore, features with a smaller aerodynamical importance, such as gills, bargeboards and wheel fairings, were taken out. See Appendix A for the detailed design of the F1 car geometry model.

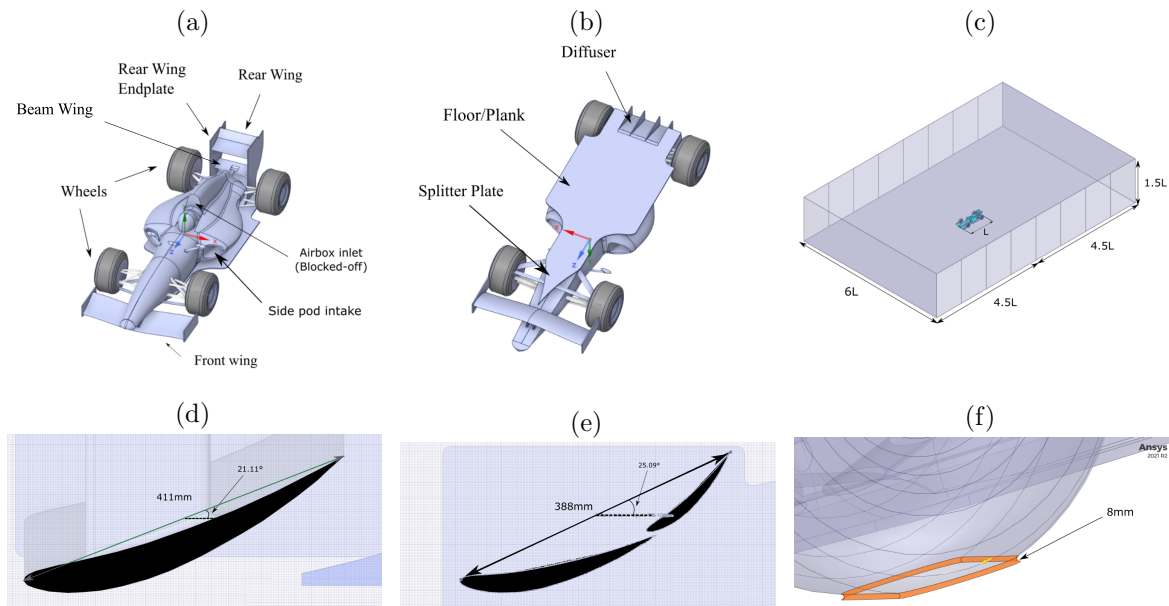


Figure 9: (a),(b) Top and bottom views of the main components of the F1 car model, (c) Domain enclosure of the car, (d) The single-element aerofoil front wing, (e) The double-element aerofoil rear wing, (f) Wheels contact patches

2.4 DISCRETISATION

Figure 10a shows the simulations domain of the aerofoil model. The aerofoil domain was discretised

based on a hybrid mesh, in which a 12-layer structured mesh close to the aerofoil surface was used to effectively capture the boundary layer effect. Further away from the aerofoil surface, tetrahedral mesh was used with a gradual increase in the size of mesh elements to reduce memory overhead. The entire mesh consisted of 1.15×10^5 cells.

Regarding the F1 domain, as shown in Figure 10b, it was discretised from converting a tetrahedral mesh into a polyhedral mesh, with a higher mesh concentration nearer to the vehicle surface. Tetrahedrons can be generated rapidly and semi-automatically, allowing implementation on complex geometries like the F1 racing car without a significant amount of ‘CAD fixing’. Conversion into polyhedral cells is a simple process by decomposition of cells into multiple sub-volumes depicted [23]. Meshing with polyhedrons lowers the numerical diffusion during calculations. With more neighbouring cells than that of the tetrahedral mesh, a faster converged solution is reached with higher accuracy, especially near high spatial gradient regions. The total cell count was about 3.50×10^6 .

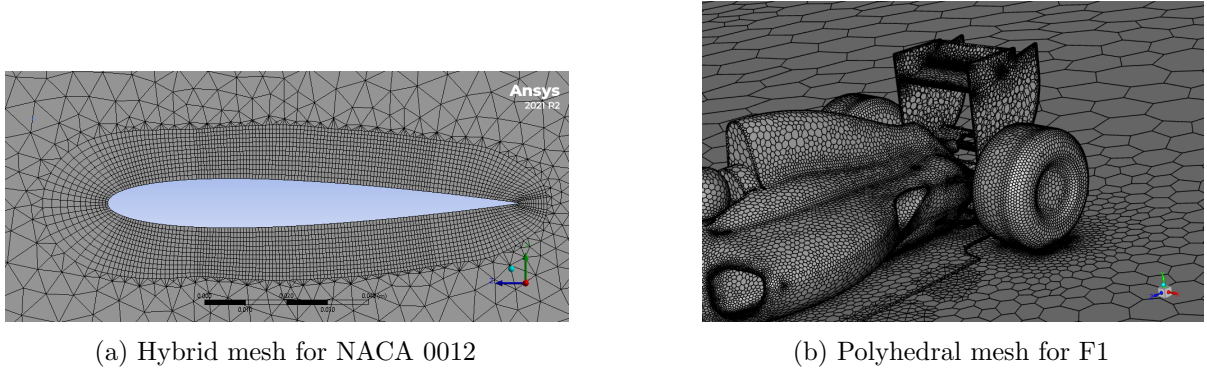


Figure 10: Discretisation of the aerofoil and F1 model

2.5 GOVERNING EQUATIONS

Two sets of governing equations were used for the fixed inertial reference frame and the non-inertial reference frame respectively, both consisting of continuity equations and Navier-Stokes (NS) equations for incompressible Newtonian flow.

2.5.1 Governing equations for the fixed frame of reference

Conservation of mass:

$$\frac{\partial \rho}{\partial t} + \vec{\nabla} \cdot (\rho \vec{u}) = 0 \quad (6)$$

Conservation of momentum:

$$\frac{\partial(\rho \vec{u})}{\partial t} + \vec{\nabla} \cdot (\rho \vec{u} \vec{u}) = -\vec{\nabla} p + \vec{\nabla} \cdot \vec{\tau} + \vec{F} \quad (7)$$

Conservation of energy:

$$\frac{\partial(\rho E)}{\partial t} + \vec{\nabla} \cdot ((\rho E + p) \vec{u}) = -\vec{\nabla} \cdot \left(\sum_j h_j J_j \right) + S_h \quad (8)$$

Equation 7 consists of the viscous term τ and external forces F . Equations 6, 7, 8 are standard NS equations for CFD applications.

2.5.2 Governing equations for non-inertial (rotating) frame of reference

Conservation of mass:

$$\frac{\partial \rho}{\partial t} + \vec{\nabla} \cdot (\rho \vec{v}_r) = 0 \quad (9)$$

Conservation of momentum:

$$\frac{\partial(\rho \vec{v}_r)}{\partial t} + \vec{\nabla} \cdot (\rho \vec{v}_r \vec{v}_r) + \rho(2\vec{\omega} \times \vec{v}_r + \vec{\omega} \times \vec{\omega} \times \vec{r}) = -\vec{\nabla} p + \vec{\nabla} \cdot \vec{\tau}_r + \vec{F} \quad (10)$$

Conservation of energy:

$$\frac{\partial(\rho E_r)}{\partial t} + \vec{\nabla} \cdot (\rho \vec{v}_r H_r) = \vec{\nabla} \cdot (k \nabla T + \vec{\tau}_r \cdot \vec{v}_r) + S_h \quad (11)$$

The governing equations for a steady rotating mesh are written in the form of relative velocity. Equation 10 consists of two additional term compared to Equation 7 for the fixed frame, the centrifugal term $2\vec{\omega} \times \vec{v}_r$ and the Coriolis term $\vec{\omega} \times \vec{\omega} \times \vec{r}$. Coriolis force arises on the test object when the reference frame rotates with respect to the inertial frame. In Equation 11, E_r , H_r and τ_r refer to the relative internal energy, relative total enthalpy and relative viscous term to E , H and τ respectively [2].

2.6 SOLVER

ANSYS Fluent was used to produce simulations and results. All simulations were run on a 64-bit cluster using a pressure-based, coupled solver that has been shown to perform well in previous studies in motorsports applications [18, 17, 16]. Convergence was deemed to be met when the mass and momentum scaled-residual errors reached 1×10^{-4} over 1,000 continued iterations. A second-order cell-based upwind discretisation scheme was applied. The Shear Stress Transport (SST) $k - \omega$ turbulence model was implemented to capture laminar separation bubbles, which have been shown to contribute towards downforce generation [9]. Constant values of $y+$ heat transfer coefficient of 300, air density of 1.225 kg/m^3 , viscosity of $1.79 \times 10^{-5} \text{ kg/ms}$ were set in all simulations. Some assumptions were made in the boundary setup. The effect of gravity was neglected. The turbulent flow around the test object was assumed to be in a steady-state.

3 RESULTS

3.1 The aerofoil model

3.1.1 Effects of different number of slots

With a pre-defined chord-to-radius ratio of 0.1 and the aerofoil length of 0.1m, a cornering radius of 1m was used in the investigation of the effect of using 4 and 8 blowing and suction slots on each side. Pressure distributions along the chord in both cases are shown in Figure 11, with a comparison against the rotating frame of reference. An additional straight-line case was simulated as a reference to demonstrate performance changes due to cornering (also included in all simulation cases).

During a corner, the pressure coefficient (C_p) of the upper and lower surfaces of the symmetrical aerofoil differentiated as the upper surface experienced a higher velocity flow. Moreover, the trailing edge experienced a lower pressure compared to that in straight freestream due to a faster exit flow generated by the curved flow field. Figures show that the blowing and suction method closely modelled the actual cornering phenomenon, particularly using 8 slots. Table 1 shows the simulation errors of C_p in both cases, in which the error significantly decreased in using 8 slots. This proves that implementing 8 slots provides a more accurate simulation, therefore it was chosen as the default number of blowing slots for the rest of the comparing cases below.

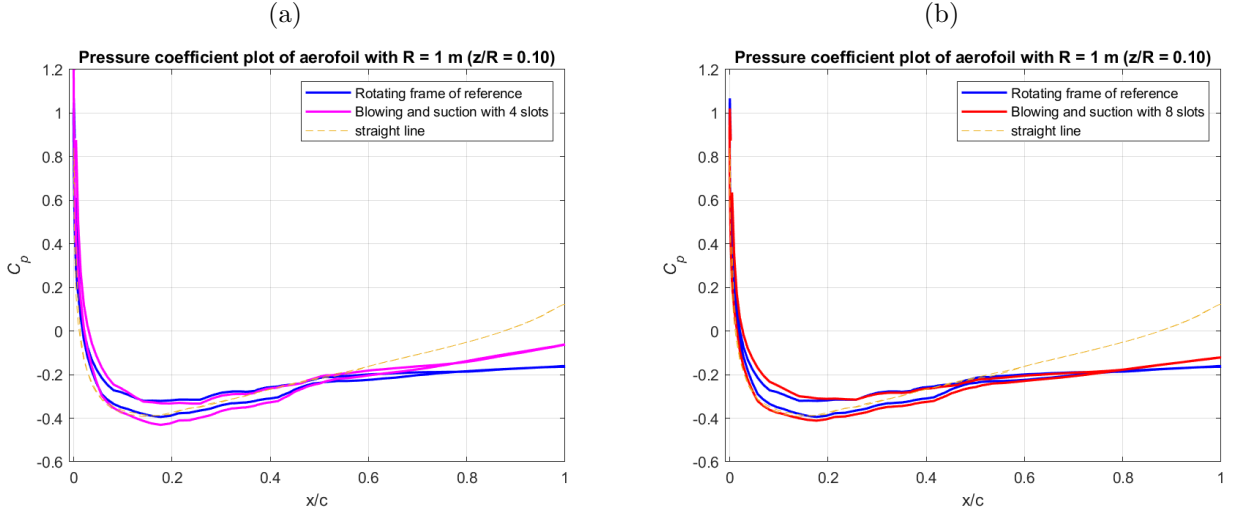


Figure 11: Pressure coefficient plotted against normalised chord length for 1m cornering radius:
(a) with 4 slots, (b) with 8 slots

	Mean absolute error	Root mean square error
Blowing and suction with 4 slots	0.0562	0.0847
Blowing and suction with 8 slots	0.0231	0.0278

Table 1: Simulation error of the aerofoil with 1m cornering radius ($z/R=0.1$)

3.1.2 Effects of reducing cornering radius

A tighter cornering situation with a chord-to-radius ratio of 0.15 was tested, corresponding to a constant cornering radius of 0.66m. C_p distribution is shown in Figure 12, which is compared directly against Figure 11b with 8 blowing slots.

A larger differentiation of C_p between the upper and lower surfaces is observed as the cornering radius decreases. Moreover, the accuracy of the blowing and suction simulation decreases with a much larger error shown in Table 2. For instance, based on the rotating mesh, C_p for both upper and lower surfaces should be the same at the normalized chord position (x/c) of 0.256, hence the intersection. Further down the chord, the upper surface experienced a higher pressure upon the intersection. Nevertheless, this effect could not be replicated using the blowing and suction model.

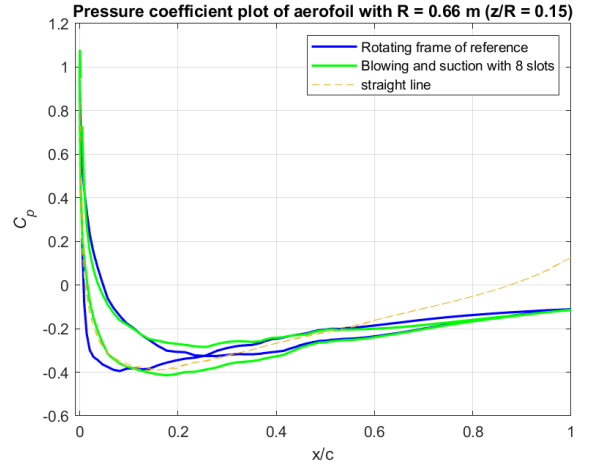


Figure 12: Pressure coefficient plotted against the normalized chord length for 0.66m cornering radius with 8 slots

	Mean absolute error	Root mean square error
Blowing and suction with 8 slots	0.0855	0.1535

Table 2: Simulation error of the aerofoil with 0.66m cornering radius ($z/R=0.15$)

3.2 The F1 racing car model

Cornering aerodynamic analysis of the F1 racing car model was divided into two sections, the global performance of the front and rear wings including the negative lift and drag coefficients (Section 3.2.1), and the 3D flow analysis of the simulated radius, pressure and vortex (Section 3.2.2). For each section, two chord-to-radius ratios of 0.10 and 0.15 were investigated. Based on the model length, they correspond to radii of 50m and 30m respectively.

A set of results based on Equation 5 was produced initially, which was discovered to have limited accuracies. Manual tuning (denoted as ‘modification’) was done additionally on the mass flow rate values (\dot{m}) to match with that in the idealised rotating mesh simulation. Both results are shown and compared below.

3.2.1 Global performance of the main components

$$C_L = \frac{L}{1/2 \rho V_{in}^2 S} \quad (12)$$

$$C_D = \frac{D}{1/2 \rho V_{in}^2 S} \quad (13)$$

The lift coefficient (C_L) and drag coefficient (C_D) are defined in Equations 12, 13, where S is the projected planform area of the front and rear wings, found to be 0.627 m^2 and 0.212 m^2 respectively. V_{in} is the flow velocity of the main inlet and L is the negative lift, which is the downforce produced by the front or rear wing. Lifts (L) and drags (D) of both wings were obtained by resolving the vertical and horizontal force components respectively, taking into account the pressure difference between upper and lower surfaces and viscous forces. Results of C_L and C_D in the case of 50m cornering radius were shown in Table 3.

Compared to the straight-line case, it is apparent that components under cornering effect result in a loss in downforce, but at the same time drag is reduced. For the front wing performance, theoretical \dot{m} in blowing and suction achieved a high accuracy of 99% and 90% in C_L and C_D respectively. Further modification only marginally improved the accuracy in C_D , and even slightly deteriorated that of C_L . On the contrary, C_L and C_D for the rear wing achieved much lower accuracies of 73% and 76% for theoretical \dot{m} , which is brought to attention that rear component are heavily affected by the aerodynamics of upstream components. There was a substantial increase of 9% and 13% in accuracies for C_L and C_D after modification.

	C_L		C_D	
	Front Wing	Rear Wing	Front Wing	Rear Wing
Straight line	1.728	1.316	0.258	0.463
Rotating frame of reference	1.584	1.217	0.222	0.422
Blowing and suction domain with theoretical \dot{m} (Percentage error)	1.597 (0.821 %)	1.537 (26.294 %)	0.243 (9.459 %)	0.520 (23.223 %)
Blowing and suction domain with modified \dot{m} (Percentage error)	1.601 (1.073 %)	1.442 (18.488 %)	0.241 (8.559 %)	0.468 (10.900 %)

Table 3: Lift and drag coefficients of main components of the F1 car model for 50m cornering radius ($z/R = 0.10$)

Table 4 shows the C_L and C_D calculated in the case of 30m cornering radius. The loss of downforce compared to vehicle in straight-line motion is more apparent during a tighter corner. Similar to the 50m radius case, in general, accuracies of C_L and C_D for both components increased after

modification, with more precise modelling of the front wing than the rear wing. However, it still exhibited a lower level of accuracy than the 50m-radius case and using theoretical \dot{m} significantly underestimated all coefficients. In particular, there was a large percentage error of -21% in C_L from the theoretical \dot{m} for the front wing. Although it was improved by 17% after modification, it was still nearly four times larger than that in Table 3.

	C_L		C_D	
	Front Wing	Rear Wing	Front Wing	Rear Wing
Straight line	1.728	1.316	0.258	0.463
Rotating frame of reference	1.574	1.083	0.225	0.372
Blowing and suction domain with theoretical \dot{m}	1.238	0.801	0.206	0.319
Percentage error	(-21.093 %)	(-26.039 %)	(-8.444 %)	(-14.247 %)
Blowing and suction domain with modified \dot{m}	1.629	1.315	0.254	0.417
Percentage error	(3.748 %)	(19.668 %)	(12.889 %)	(12.097 %)

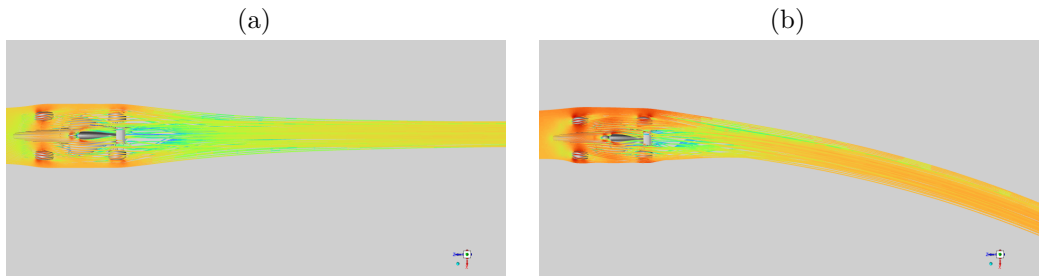
Table 4: Lift and drag coefficients of main components of the F1 car model for 30m cornering radius ($z/R = 0.15$)

3.2.2 3D Flow analysis (Validation for Radius, Pressure and Vortex)

Radius Validation It is important to examine whether the blowing and suction wind tunnel is modelling the assigned cornering radius precisely. Firstly, the 50m radius was validated, with streamlines of relative velocities from different models visualised in Figure 14. To calculate the simulated cornering radius from each streamlines plot, the general equation of a 2D circle (Equation 14) was used, with 3 unknowns h, k and radius R .

$$(x - h)^2 + (y - k)^2 = R^2 \quad (14)$$

Through obtaining 3 arbitrary points from a streamline passing through the nose of the F1 racing car model, 3 equations with 3 unknowns can be constructed to deduce R . Results of radii corresponding to Figure 14b, c, d are shown in Table 5. Blowing and suction under theoretical \dot{m} was in fact simulating a radius of 40.6m, which was a huge overshoot in cornering curvature caused by an excessive amount of blowing and suction. After reducing the \dot{m} in modification, a more accurate radius of 52.3m was established. It is also noteworthy that for both blowing and suction simulations in Figure 14c, d, the trailing flow was accelerated near the end of the domain outlet, particularly using the theoretical \dot{m} . Since it occurred in the far-field, the direct influence on the vehicle was little.



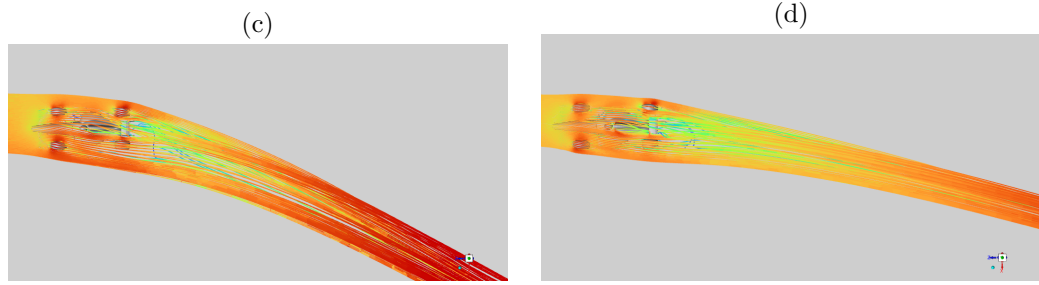


Figure 14: Relative velocity streamlines of the F1 car model in (a) Straight line, and for 50m cornering radius ($z/R = 0.10$) in: (b) Rotating reference frame, (c) Blowing and suction with theoretical \dot{m} , (d) Blowing and suction with modified \dot{m}

Simulation case	Radius (m)	Percentage error (%)
Rotating frame of reference	50.0	-
Blowing and suction with theoretical \dot{m}	40.6	-18.8
Blowing and suction with modified \dot{m}	52.3	4.6

Table 5: Radius validation for the F1 car model in a 50m corner ($z/R = 0.10$)

Streamlines of relative velocities for the 30m-cornering radius case were visualised in Figure 15. In general, compared to Figure 14b, c, d, they all show a larger curvature demonstrating a tighter corner, with a smaller magnitude of relative velocity characterised by the lighter streamline colour. Table 6 shows the corresponding radius calculations, in which again, an exaggerated cornering curvature of 21m was obtained using theoretical \dot{m} , and greatly improved after modification, achieving 29.8m. Similarly, there was a flow acceleration closer to the domain outlet when using the blowing and suction method, as shown in Figure 14b, c.

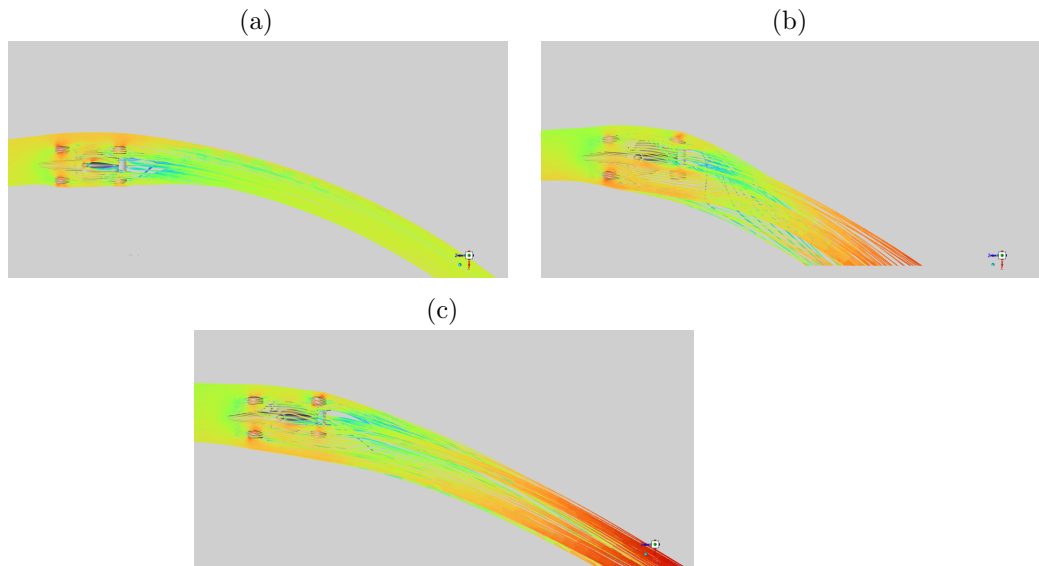


Figure 15: Relative velocity streamlines of the F1 car model for 30m cornering radius ($z/R = 0.15$): (a) Rotating reference frame, (b) Blowing and suction with theoretical \dot{m} , (c) Blowing and suction with modified \dot{m}

Simulation case	Radius (m)	Percentage error (%)
Rotating frame of reference	30.0	-
Blowing and suction with theocratical m	21.0	-30.0
Blowing and suction with modified m	29.8	-0.67

Table 6: Radius validation for the F1 car model in a 30m corner ($z/R = 0.15$)

Pressure Validation Pressure coefficients of the F1 racing car model were analysed both globally and locally. A plot of the entire surface pressure of the vehicle was generated for each simulation. In particular, the pressure of the front wing was investigated as it is a major component generating approximately 30% of the total downforce of the F1 car [6]. An iso-plane was created normal to the front wing, as shown in Figure 16, to observe the pressure away from the front wing surface. A sectional polyline (denoted as the green line in Figure 16) was created at the outboard normalised position (x/c) of 1.25 of the front wing to observe the surface pressure distribution along the line.

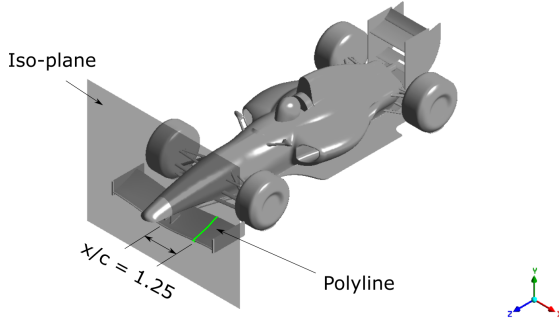


Figure 16: Characteristics considered for the pressure validation

Figure 17 shows the pressure coefficient analysis of the 50m-cornering radius case. In general, the pressure contours of the two blowing and suction cases closely matched with that of the idealised rotating reference frame. It was noticeable that lowered surface pressure coefficients around the engine intake, rear wing end-plates and the left front wheel were obtained when the theoretical \dot{m} was applied. It means that the theoretical \dot{m} was excessive, resulting in a larger flow velocity. The reduction of \dot{m} after modification slightly increased the pressure in those areas (Figure 17a(iii)).

Figure 17c shows the surface pressure distribution of the front wing along the polyline, indicating a highly accurate simulation using the blowing and suction method, especially after modification. Pressures away from the front wing surface on the iso-plane from all simulations were demonstrated in Figure 17b. Asymmetrical pressure distribution was observed due to cornering, in which the inner side was perceived as a convex surface, causing a rearward expansion and subsequently aiding a flow acceleration, and vice versa for the outer side. Combining with the radial pressure gradient, this resulted in a higher pressure on the outer side from the centre of rotation. Although the asymmetry was modelled by both blowing and suction cases, the cornering effect was exaggerated away from the upper surface, which could not be corrected by modification. Moreover, the overall pressures away from the surface in both simulations were lower than the idealised rotating simulation.

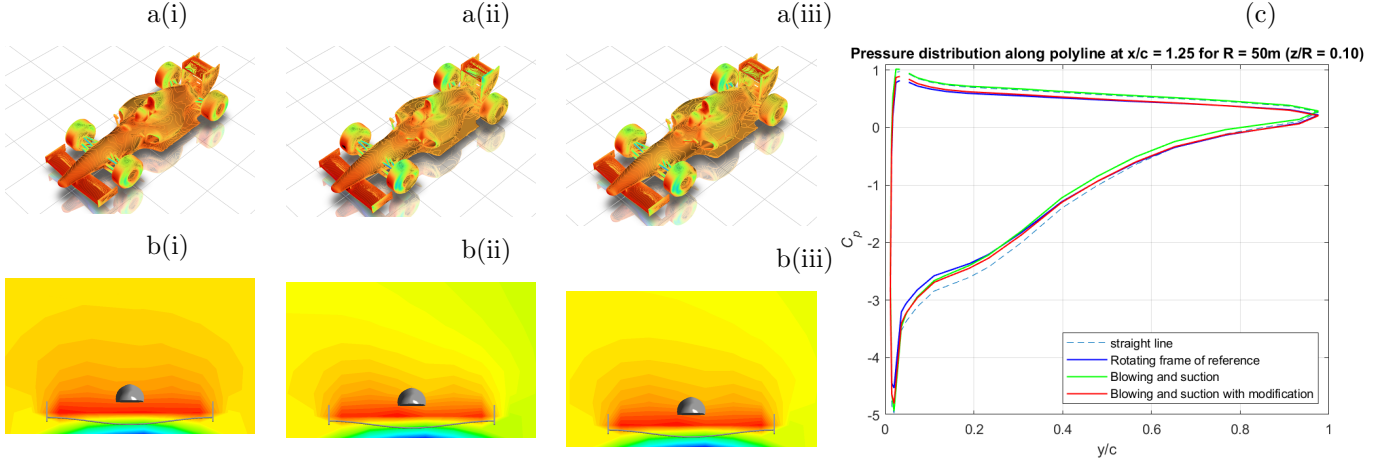


Figure 17: Pressure validation of the F1 car model in 50m corner ($z/R = 0.10$): (a) Pressure coefficient contour (b) Iso-plane pressure for (i) rotating reference frame, (ii) blowing and suction with theoretical \dot{m} , (iii) blowing and suction with modified \dot{m} , (c) Pressure distributions along polyline at $x/c = 1.25$.

Pressure coefficient analysis of the 30m-cornering radius case is shown in Figure 18. A tighter cornering radius results in overall higher surface pressure. It is because, given a constant angular velocity, the tangential velocity is smaller for a smaller cornering radius. It is visualised by the overall darker colour of the pressure contours (Figure 18a). Using the theoretical \dot{m} lowered the pressure coefficients of similar areas to that in the 50m-radius case, which was also improved after modification. According to the surface pressure distribution of the front wing (Figure 18c) and the iso-plane visualization (Figure 18b), compared to the idealised simulation, both figures show that there was an underestimation of pressure at and especially away from the surface when theoretical \dot{m} was applied. Despite an apparent improvement after modification, the non-overlapping plot in Figure 18c and the lighter colour of Figure 18b(iii) demonstrated that simulations were not able to achieve the same level of accuracy compared to the 50m-radius case.

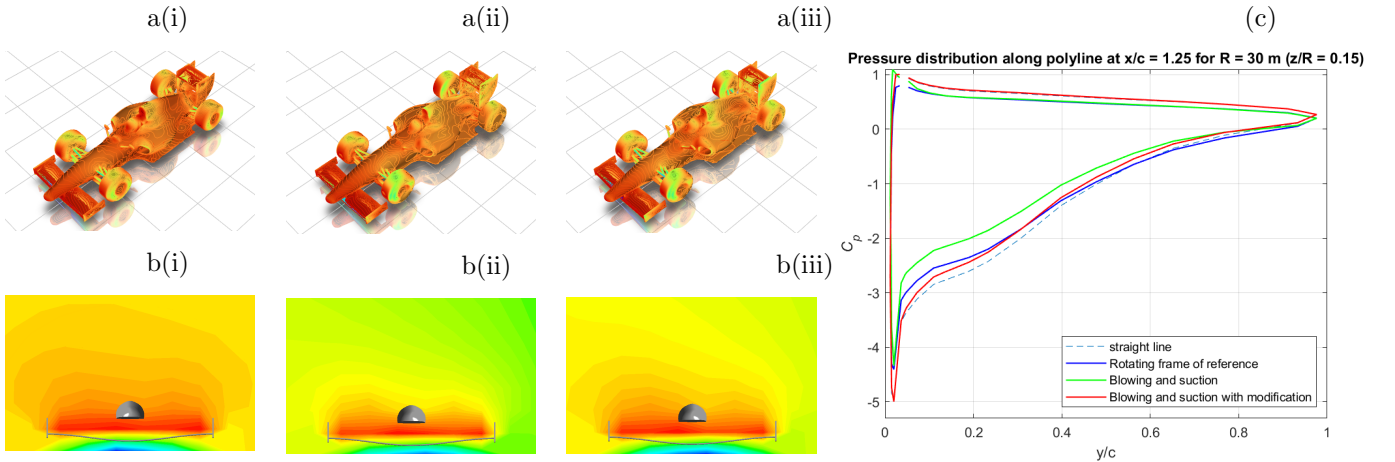


Figure 18: Pressure validation of the F1 car model in 30m corner ($z/R = 0.15$): (a) Pressure coefficient contour (b) Iso-plane pressure for (i) rotating reference frame, (ii) blowing and suction with theoretical \dot{m} , (iii) blowing and suction with modified \dot{m} , (c) Pressure distributions along polyline at $x/c = 1.25$.

Vortex Validation Vortices and vortex layers are aerodynamic characteristics highly associated with the performance of an F1 racing car. They are important in direct downforce generation and act as air curtains to seal off low-pressure areas [3]. Figure 19 demonstrates the shape of vortices created during a corner under the Q-criterion, with the absolute helicity values plotted using a heatmap on the vortex iso-surface. The absolute helicity is a scalar quantity defined as the dot product between velocity and vorticity vectors, which is utilised to locate the core of streamline vortices.

During a corner, the wake structure of the vehicle is expected to become asymmetrical, where flow structures of the outer side would be dominant in the wake region, particularly due to an increase in strength of the outboard C-pillar vortex [16]. Even though the vehicle body would have a straightening effect on the flow, the trailing wake would still tend towards the direction of the freestream flow. Hence, the trailing vortices would be curved following the shape of trailing streamlines. These curved trailing vortices at the rear wing were observed in Figure 19, indicating that vortices were correctly captured by blowing and suction simulations. Improvements upon modification were visually insignificant in both radii. Although differences in Q-criterion were not apparent between the 50m-radius and 30m-radius cases, smaller values of the helicity for the 50m- corner indicated that trailing vortices are more aligned with the streamwise flow compared to the tighter corner.

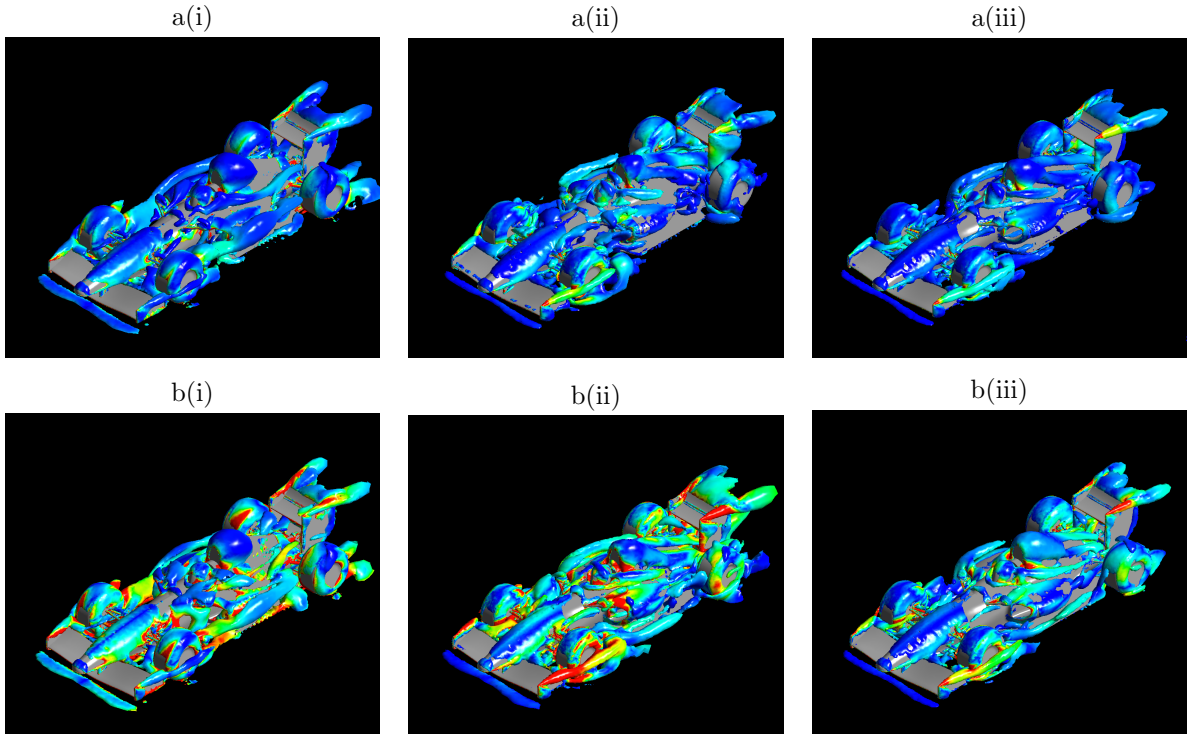


Figure 19: Q-criterion vortex core shape merging visualisation with absolute helicity for (a) 50m corner, (b) 30m corner in: (i) rotating reference frame, (ii) blowing and suction with theoretical \dot{m} , (iii) blowing and suction with modified \dot{m}

4 DISCUSSION

4.1 Performance on the aerofoil

The purpose of simulating an aerofoil model is to demonstrate the chordwise effect due to blowing and suction simulations with a simpler case. The presence of non-uniform radial pressure in wind tunnels is a physical limitation ceasing it from producing an exact cornering condition. Yet, results proved that the blowing and suction simulation is capable to replicate cornering to a high level

of accuracy under general cornering curvatures ($z/R \approx 0.1$).

The effect of using a different number of blowing slots was evaluated. With the estimation of a possible number of slots from the dimension of the wind tunnel design, 8 slots in each sidewall were considered to be the maximum case. Results in Section 3.1.1 demonstrated the significant improvement in accuracy when using a greater number of slots. In an actual cornering scenario, the velocity components across the vehicle width are varied by $\omega R \sin(\theta)$, implying a continuous change in crosswind velocity as the vehicle travels through the corner. Increasing the number of blowing and suction slots provides a higher resolution in modelling finite element crosswind, hence it is preferable to have more slots to obtain higher accuracy. However, as previously mentioned, the number of slots has to be compromised with the actual construction feasibility and cost. Future work can be dedicated to investigating the optimised number of slots with consideration of different factors.

In terms of the cornering radius comparison (Section 3.1.2), a larger error was observed in a larger curvature ($z/R = 0.15$). It is due to air diffusion, causing a different flow velocity at the wall and flow experienced by the model during a tighter cornering condition. It is further discussed in Section 4.2 below.

4.2 Performance on the F1 car

The F1 car model simulation demonstrated a more complex case, which is also the intended purpose for the blowing and suction wind tunnel. In general, results obtained from blowing and suction simulations using the theoretical mass flow rates deviated from idealised results, and significantly improved after modification. Theoretical mass flow rates were derived from Equation 5, which is based on the path of the vehicle's centre of gravity. However, it did not take into account the presence of a blowing distance between the sidewall and the vehicle model in the simulation that would result in an occurrence of the turbulent diffusion. When the air in the main inlet mixes with the air introduced by blowing, turbulent flow mixing occurs on the macroscale. A macroscale refers to larger revolving flows (vortices) produced due to the instability of the average flow, subsequently causing energy to cascade in microscale [7]. This effect is amplified in simulations with a smaller cornering radius, where the blowing speed is relatively larger compared to the freestream flow speed. Blowing and suction velocities at the sidewall therefore deviate further away from the experienced velocities. This also explains the larger percentage errors observed in the 30m-radius simulations in both aerofoil and F1 models compared to that of 50m-radius simulations.

Therefore, the above issue was addressed by modifications, where each mass flow rate value was replaced with the one used in the corresponding idealised rotating simulation. Significant improvements in accuracies were obtained, indicating a more precise replication of a true cornering condition using the blowing and suction method. This manual tuning is also a feasible approach in practice for the wind tunnel, in which inlet velocities and mass flow rates on each blowing and suction slot can be easily adjusted by varying the fan speeds. To further improve the robustness of the tuning process for simulating various corners, the use of machine learning and optimisation techniques are suggested for future implementation.

In validating the iso-planes of the front wing, there were underestimations in the pressure away from the surface by blowing and suction in both cornering radii, regardless of modifications. One of the reasons behind this is due to the assumption of constant tangential velocity ωR during a corner. To model a varying tangential velocity $\omega R \cos(\theta)$, blowing channels can be implemented at an angle towards the direction of the inlet. This effectively decreases the inlet velocity and eliminates the underestimation of the pressure away from surfaces.

One notable trend in the main components performance analysis is that C_L , C_D of the rear wing are prone to errors. It is due to turbulence and vortices introduced by upstream components, affecting the flow quality for the rear wing [18]. Therefore, force coefficients of the rear wing obtained

from whole-car modelling are not reliable indications of the simulation accuracy. To better model the cornering effects of downstream components, it is suggested that they should be simulated individually in future research.

4.3 Limitation and Future Work

In this primary proposal for the blowing and suction wind tunnel, results suggest that the blowing and suction method is accurate to a large extent in simulating cornering conditions under relaxed cornering curvatures, indicating the feasibility of implementing this domain in the construction of a wind tunnel. However, limitations in precisely replicating the aerodynamics for tighter corners exist. Given the large expenses and difficulty in constructing a wind tunnel, to make it cost-effective, further dedications into domain modification and computational results validations are required to improve simulation performances, especially for tighter corners. In addition to suggestions mentioned in Section 4.1, 4.2, elements that were not taken into account during designing and simulation are listed below, which can be considered in future work.

Firstly, regarding the conceptual design, position and geometry of blowing and suction ducts can be further investigated to account for the effect of gravity in the vertical duct sections and pressure loss due to the four corners of each duct. Furthermore, this research assumed that the vehicle centre line was aligned with the tangent of the corner, which is rarely happening in present F1 races. Therefore, side-slip angles should be taken into account by offsetting the blowing and suction speed accordingly. Similarly, wheel turning angles can also be integrated into the vehicle CAD model to replicate the wheel dynamics during a corner. Since turned wheels might then produce large wakes that would affect other components, a separate investigation of any component of interest is suggested. In addition, moving ground boundary conditions can also be applied to the simulation solver. Aerodynamic effects due to the relative motion between the vehicle and the ground can then be simulated, especially for ground boundary layers [8]. Lastly, the model discretisation can be further refined to F1 teams standard, typically ranging between $50\text{--}200 \times 10^6$ cells [18].

5 CONCLUSION

This paper is the first to propose the idea of designing a blowing and suction wind tunnel to simulate cornering effects mainly in race tracks. Based on a fixed frame of reference, blowing and suction boundary conditions were applied to both aerofoil and F1 racing car simulations. It is concluded that this method obtained a high level of accuracy in simulating standard F1 track corners, but invites improvements for tighter cornering simulations. Using a greater number of slots mimics the closest results to the idealised rotating domain, subsequently trading off with construction complexity. Improvements in modelling the desired surface pressures and path curvatures were demonstrated after adjusting the mass flow rates based on the rotating domain. The adjustments attenuate the turbulent flow mixing effect. Investigating the construction and geometries of blowing and suction ducts, implementing angled blowing channels and moving belts are sources of potential future developments.

6 ACKNOWLEDGMENT

The author would like to acknowledge the support of Dr Thomas C S Rendall, whose advice and guidance throughout the project have been invaluable.

REFERENCES

- [1] F1 track data. <https://www.formula1.com/en/information.singapore-marina-bay-street-circuit.7LXNQUCHTyR5yMQP1Ik7Lv.html>.
- [2] Flows with rotating reference frames. https://mae.iith.ac.in/ansys/files/scientific/fluent_tut/theoryguide_Flows%20with%20rotating%20refrences%20frames.pdf.
- [3] Mulsanne's corner, vortex. <http://www.formula1-dictionary.net/vortex.html>.
- [4] The slotted wall revolutionizes transonic research. <https://history.nasa.gov/SP-440/ch5-9.htm>.
- [5] Stability tunnel. http://crgis.ndc.nasa.gov/historic/Stability_Tunnel.
- [6] B. Agathangelou and M. Gascoyne. Aerodynamic design considerations of a formula 1 racing car. Technical report, SAE Technical Paper, 1998.
- [7] J. Bergström. Cfd for mixing efficiency in commercial and industrial advanced air oxidation, 2018.
- [8] C. Collin, T. Indinger, and J. Müller. Moving ground simulation for high performance race cars in an automotive wind tunnel-cfd approach on moving belt dimensions. *International Journal of Automotive Engineering*, 8(1):15–21, 2017.
- [9] J. Correia, L. Roberts, M. Finnis, and K. Knowles. Scale effects on a single-element inverted wing in ground effect. *The Aeronautical Journal*, 118(1205):797–809, 2014.
- [10] S. Diasinos. The aerodynamic interaction of a rotating wheel and a downforce producing wing in ground effect. *School of Mechanical and Manufacturing Engineering*, 2009.
- [11] B. Goffert, M. A. Ortega, and J. B. P. Falcão. Numerical study of wall ventilation in a transonic wind tunnel. *Journal of Aerospace Technology and Management*, 7:81–92, 2015.
- [12] A. Gordes. Process for simulating curved airflow on wheeled vehicles in fluid channels with a straight measuring section. Patent No. EP1610111A2, Germany, 2005.
- [13] P. Gregory. *Flow over a body of revolution in a steady turn*. PhD thesis, 2006.
- [14] M. A. G. Hernández, A. I. M. López, A. A. Jarzabek, J. M. P. Perales, Y. Wu, and S. Xiaoxiao. Design methodology for a quick and low-cost wind tunnel. *Wind tunnel designs and their diverse engineering applications*, 1:3–26, 2013.
- [15] C. W. Hirt, A. A. Amsden, and J. Cook. An arbitrary lagrangian-eulerian computing method for all flow speeds. *Journal of computational physics*, 14(3):227–253, 1974.
- [16] J. Keogh, T. Barber, S. Diasinos, and G. Doig. The aerodynamic effects on a cornering ahmed body. *Journal of Wind Engineering and Industrial Aerodynamics*, 154:34–46, 2016.
- [17] J. Keogh, T. J. Barber, S. Diasinos, and G. Doig. Techniques for aerodynamic analysis of cornering vehicles. In *18th Asia Pacific Automotive Engineering Conference Proceedings: Melbourne, Australia*, 2015.
- [18] J. Keogh, G. Doig, and S. Diasinos. Flow compressibility effects around an open-wheel racing car. *The Aeronautical Journal*, 118(1210):1409–1431, 2014.
- [19] M. Mulkens and A. Ormerod. Steady-state experiments for measurements of aerodynamic stability derivatives of a high incidence research model using the college of aeronautics whirling ann. Technical report, Citeseer, 1990.
- [20] M. Nakagawa, S. Kallweit, F. Michaux, and T. Hojo. Typical velocity fields and vortical structures around a formula one car, based on experimental investigations using particle image velocimetry. *SAE Int. J. Passeng. Cars-Mech. Syst.*, 9(2):754–771, 2016.
- [21] K. Nara, M. Tsubokura, and J. Ikeda. A numerical analysis of unsteady aerodynamics of formula car during dynamic cornering motion. In *32nd AIAA applied aerodynamics conference*, page 3138, 2014.
- [22] Y. Okada, T. Nouzawa, S. Okamoto, T. Fujita, T. Kamioka, and M. Tsubokura. Unsteady vehicle aerodynamics during a dynamic steering action: 1st report, on-road analysis. Technical report, SAE Technical Paper, 2012.
- [23] M. Sosnowski, J. Krzywinski, K. Grabowska, and R. Gnatowska. Polyhedral meshing in numerical analysis of conjugate heat transfer. In *EPJ Web of Conferences*, volume 180, page 02096. EDP Sciences, 2018.
- [24] W. Toet. Aerodynamics and aerodynamic research in formula 1. *The Aeronautical Journal*, 117(1187):1–26, 2013.
- [25] M. Tsubokura, Y. Ikawa, T. Nakashima, Y. Okada, T. Kamioka, and T. Nouzawa. Unsteady vehicle aerodynamics during a dynamic steering action: 2nd report, numerical analysis. *SAE International Journal of Passenger Cars-Mechanical Systems*, 5(2012-01-0448):340–357, 2012.

APPENDIX A: DETAILED GEOMETRY OF THE F1 CAR MODEL

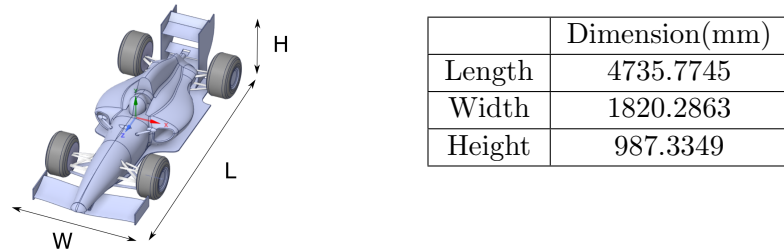


Figure 20: Full dimensions of the F1 car model

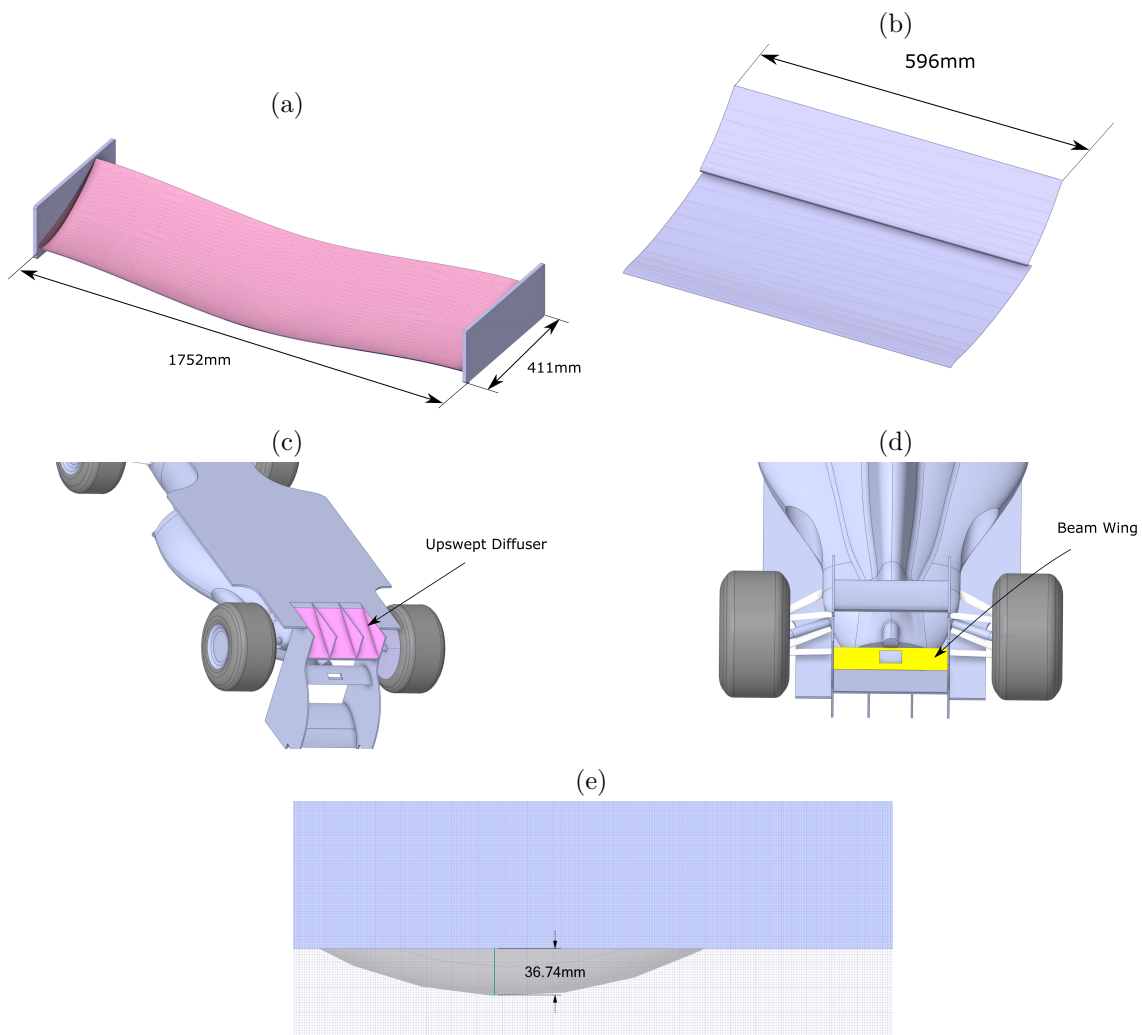


Figure 21: (a) Front wing dimensions, (b) Rear wing dimensions, (c) Upswept diffuser, (d) Beam wing, (e) Ground clearance

Total surface area	2.331 E7 mm ²
Total volume	1.721 E9 mm ³
Centre of gravity	(0, 390, -2519)
Moment of Inertia	1.319 E16 mm ⁵

Table 7: Mass properties and others

APPENDIX B - DETAILED VISUALISATION OF RELATIVE VELOCITY STREAMLINES

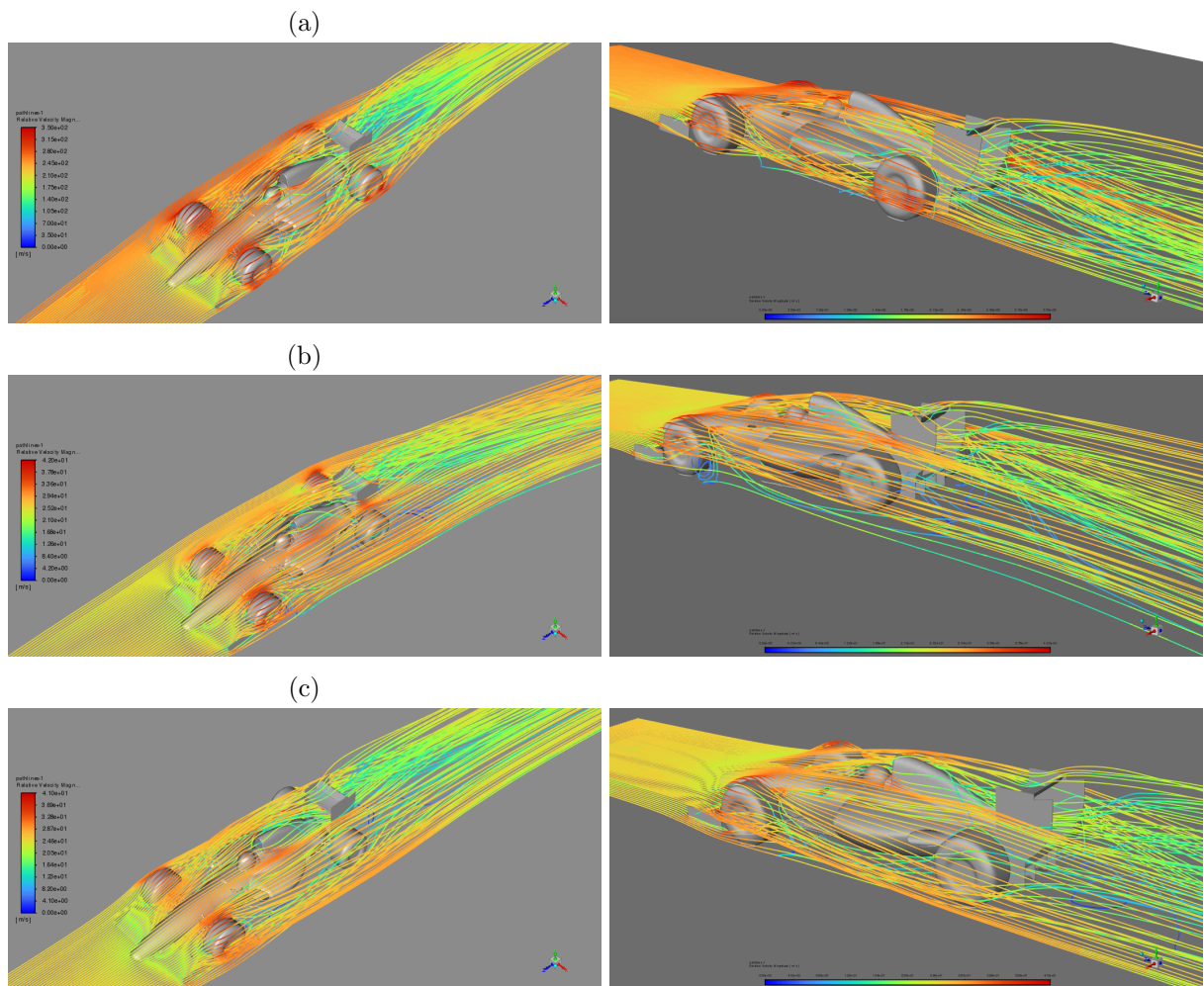


Figure 22: Relative velocity streamlines for 50m cornering radius: (a) rotating reference frame, (b) blowing and suction with theoretical \dot{m} , (c) blowing and suction with modified \dot{m}

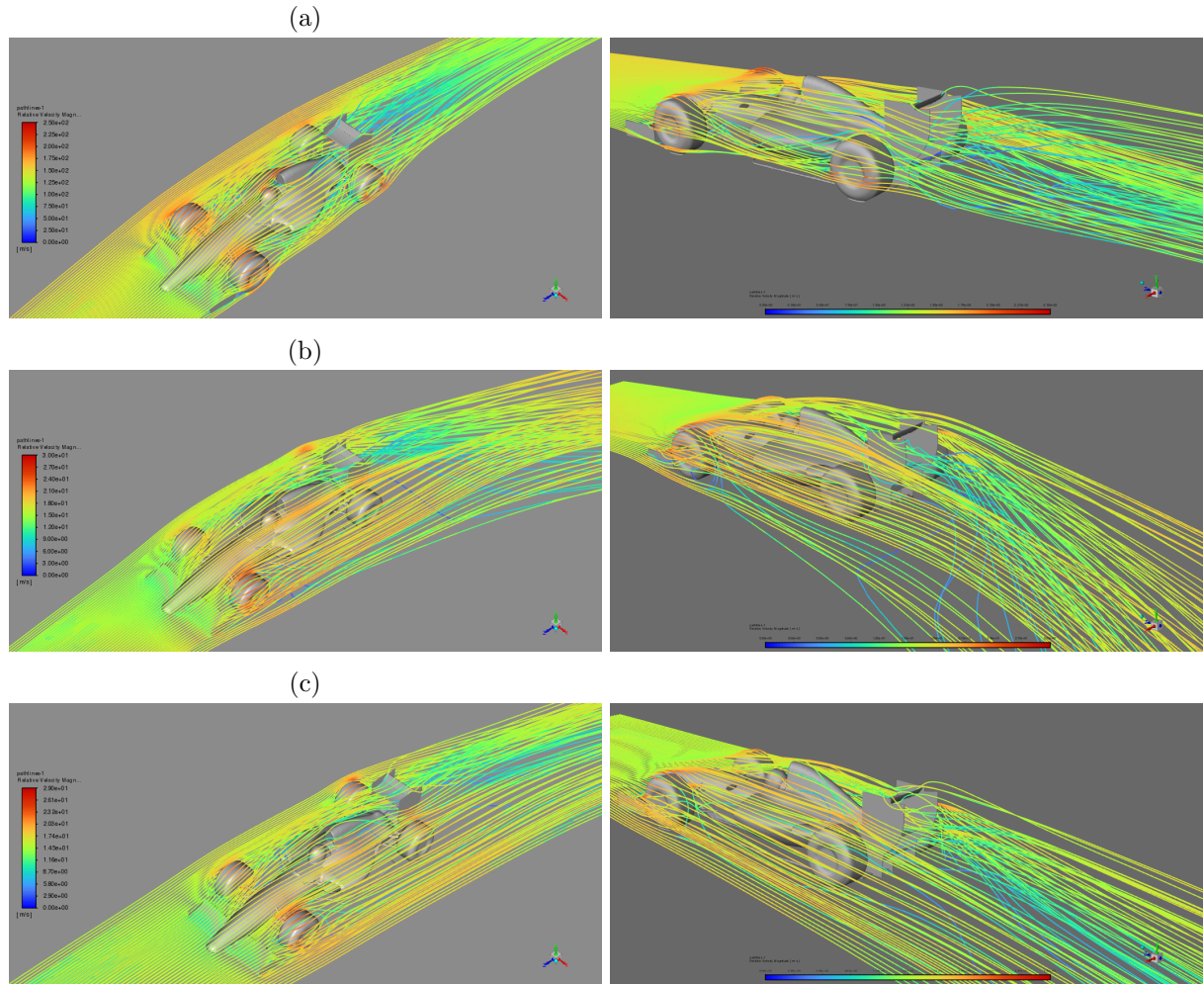


Figure 23: Relative velocity streamlines for 30m cornering radius: (a) rotating reference frame, (b) blowing and suction with theoretical \dot{m} , (c) blowing and suction with modified \dot{m}